chemengineering

MDPI

Article

Efficiency of Mechanochemical Ball Milling Technique in the Preparation of Fe/TiO_2 Photocatalysts

Shabnam Taghipour [1,2], King-Lun Yeung [1,3,4,*] and Behzad Ataie-Ashtiani [2]

[1] Department of Chemical and Biological Engineering, The Hong Kong University of Science and Technology, Clear Water Bay, Kowloon, Hong Kong
[2] Department of Civil Engineering, Sharif University of Technology, Tehran P.O. Box 11155-9313, Iran
[3] Division of Environment and Sustainability, The Hong Kong University of Science and Technology, Clear Water Bay, Kowloon, Hong Kong
[4] HKUST Shenzhen-Hong Kong Collaborative Innovation Research Institute, Futian, Shenzhen 518000, China
* Correspondence: kekyeung@ust.hk

Abstract: Rapid population growth and widespread industrialization are the main contributing factors to the increasing contamination of the world's diminishing freshwater resources. This work investigates Fe/TiO_2 as an efficient and sustainable photocatalyst for treating organic micropollutants in water. The photocatalysts prepared by these mechanochemical methods used a high-energy ball milling technique to manipulate Fe/TiO_2's structural, optical, and catalytic properties for the photo-oxidation of 2,4-Dichlorophenol (2,4-DCP). Doping with iron effectively reduced the band gap of rutile TiO_2 from 3 to 2.22 eV. By reducing the ball/powder ratio from 34 to 7, the removal efficiency of 2,4-DCP increased from 65.2 to 84.7%. Measuring the TOC indicated 63.5 and 49.4% mineralization by Fe/TiO_2-7 and rutile TiO_2, respectively, after 24 h. The energy yields for the Fe/TiO_2 and rutile TiO_2 were 0.13 and 0.06 g 2,4-DCP/kW h, respectively.

Keywords: TiO_2/Fe; photocatalyst; doping; ball milling; efficiency

Citation: Taghipour, S.; Yeung, K.-L.; Ataie-Ashtiani, B. Efficiency of Mechanochemical Ball Milling Technique in the Preparation of Fe/TiO_2 Photocatalysts. *ChemEngineering* **2022**, *6*, 77. https://doi.org/10.3390/chemengineering6050077

Academic Editors: Alírio E. Rodrigues and Andrew S. Paluch

Received: 3 August 2022
Accepted: 2 September 2022
Published: 2 October 2022

1. Introduction

Global climate change, population growth, and urbanization will see more than four billion people suffer water stress for at least one month each year by 2050 [1,2]. Moreover, decades of unbridled agricultural and industrial expansion have heavily polluted lakes, rivers, and aquifers with heavy metals, chemicals, pesticides, herbicides, and pharmaceuticals that are detrimental to human health and the environment [3–5]. Among the emerging pollutants, chlorophenols pose the biggest challenge, being persistent and refractory toxicants that bioaccumulate in the food chain. In addition, their wide use in pesticides, herbicides, fungicides, dyes, and pharmaceuticals [6,7] means they can be found extensively in the environment [8].

The chemical compound 2,4-dichlorophenol (2,4-DCP) is widespread, and due to its toxicity, carcinogenicity, and mutagenicity, it is a priority pollutant of the US Environmental Protection Agency (EPA) [9]. In addition, conventional water and wastewater treatment processes are ineffectual [10–12] at treating it, as demonstrated by its increasing occurrence in drinking water at levels exceeding the permissible concentrations of 0.5 ppm [6]. Thus, providing the impetus to develop more efficient treatment technologies such as advanced oxidation processes (AOP) that include photocatalysis [13], UV/H_2O_2 [14], UV/O_3 [15], UV/H_2O_2/O_3 [16], and Fenton/sonolysis methods [17].

Photocatalysis is attractive as it can harness light, particularly sunlight, to generate reactive radical species to degrade pollutants. It provides a low cost, efficient, and sustainable remediation method for treating recalcitrant contaminants [18–20]. TiO_2 photocatalysts are popular due to their relatively low cost, excellent durability, superb chemical stability, and high electron transport [21]. A critical shortcoming of TiO_2 is its wide bandgap, which

limits its light utilization to UV wavelengths [22]. Introducing foreign atoms such as Zn [23], Gd [24], Cu [25], Lu [26], and Al [27] can narrow its bandgap, and iron proved to be the most promising [28,29]. Iron's ionic radii, comparable to Ti^{4+}, are readily inserted into TiO_2's crystal lattice. Iron is also inexpensive and non-toxic compared to the other dopants.

The mechanochemical catalyst preparation process affords a simple, inexpensive, and green preparation of the photocatalysts [30]. This technology can help to reduce particle sizes, which plays a vital role in improving photocatalytic performance and can produce nanoparticles of a large surface area that are enriched in oxygen-containing functional groups [31]. In mechanochemical synthesis, the type of ball mill (e.g., zirconium dioxide), nature of the milling material [32], and milling speed and time [33] are crucial variables. An appropriate ball-to-powder weight ratio (B/P) is another critical parameter in high-energy ball milling. A high B/P sees more ball-to-ball impact and inefficient milling [24], while a very low B/P from overfilling reduces grinding [34]. Prior studies have often neglected the effects of ball sizes when studying B/P, which will be considered in our study of Fe/TiO_2 photocatalyst preparation and its impact on Fe^{3+} insertion and the subsequent structure, morphology, optical, and photocatalytic properties of the photocatalysts.

2. Materials and Methods

2.1. Materials

Titanium (IV) oxide, rutile (99.5% trace metals basis, CAS number: 1317-80-2), and iron (III) nitrate nonahydrate (≥98%, CAS number: 7782-61-8) catalyst precursors and 2,4-dichlorophenol (99%, CAS number: 120-83-2) were purchased from Sigma-Aldrich and used without further purification. The 2,4-DCP solutions were in deionized distilled water.

2.2. Fe/TiO_2 Photocatalysts

The Fe/TiO_2 catalysts were synthesized in a dry planetary ball mill (PBM-0.4A) at room temperature in air. Three catalyst batches were milled at B/P = 34, 17, and 7 from a powder mixture of 5 wt.% Fe(III) and 95 wt.% TiO_2. Briefly, the Fe/TiO_2-34 was obtained by milling 2.5 g catalyst precursor mixture with zirconia beads of 15 mm (2), 12 mm (8), 8 mm (6), and 5 mm (42) in size; the Fe/TiO_2-17 was prepared by milling 5 g catalyst precursor mixture; and the Fe/TiO_2-7 was milled from 5 g catalyst precursor mixture with 8 mm (6) and 5 mm (42) beads. The milling speeds and durations were kept at 400 rpm and 10 h, respectively. The direction of the milling rotation reversed every 10 min. Before conducting photocatalytic reaction, the catalyst was dissolved in 15 mL DDI water and then centrifuged (5000 rpm, 3 min) to remove the possible iron ions on its surface. The catalyst was then dried at 65 °C.

2.3. Catalyst Characterization

The catalysts' structures, morphologies, and surface textures were determined by X-ray diffraction (XRD), scanning electron microscopy (SEM), and nitrogen physisorption. The powder XRD was conducted in a PANalytical X-ray Diffractometer, Model X'pert Pro, using 2 kW Cu-Kα X-ray radiation with a graphite monochromator at a 1.5406 Å wavelength and a 7 degrees/min scan rate. The crystal size was determined using the Scherrer equation (Equation (1)) by taking the average of the dominant peaks in the diffraction data [35,36], as follows:

$$D_S = \frac{K\lambda}{\beta_D cos\theta} \quad (1)$$

where, D_s is the crystal size (nm), K is the shape factor, β_D is FWHM, λ is the wavelength of the CuKα radiation (1.5406 Å), and θ stands for the angle of the XRD. K is generally considered to be 1.0 for spherical particles.

The SEM imaging was performed using a JEOL JSM-7100F at 15 kV and 1.1 nm resolution on finely dispersed catalyst powder on a clean silicon wafer. Precautions were taken to minimize sample charging by using conductive carbon tape for sample-mounting the aluminum holder and sputtering the sample with a thin gold layer. The nitrogen physisorp-

tion isotherms of the catalysts were obtained using a Belsorp mini X (MicrotracBEL Inc., Haan, Germany). Herein, the powder catalyst was outgassed at 150 °C for 6 h before taking measurements, and the Barrett–Joyner–Halenda (BJH) model was used to determine the pore size distribution.

The catalysts' surface compositions were analyzed with a Kratos X-ray Photoelectron Spectrometer with a monochromatic Al Ka X-ray source at 1486.6 eV and an X-ray power of 150 W. The binding energy (BE) was referenced to the C 1s signal at 284.8 eV. The catalysts were further analyzed with a UV-vis NIR spectrometer (Perkin Elmer, Lambda 950) for their optical properties and band gap energies. The Raman spectra of the catalysts were collected by a Renishaw InVia Raman spectrometer equipped with a notch filter up to 100 cm^{-1} and a 100 mW Ar-laser (514 nm) as an excitation source at two scans and 30 s acquisition times under room temperature.

2.4. Photocatalytic Oxidation Reaction

Figure 1 displays the photoreactor for the batch photocatalytic oxidation of the 2,4-DCP. It consisted of a quartz tube reactor placed equidistant (10 mm) from three 6 W GE F6T5 35 lamps. The light from the lamps was filtered by a 3 mm thick polycarbonate UV-cutoff filter to remove wavelengths of <400 nm. The photoreactor setup was placed inside a stainless-steel isolation box to avoid ambient lighting. A pair of DC fan circulated air and maintained a temperature of 25 °C. A 2,4-DCP stock solution (16 mg/L) was diluted to 4.08 mg/L, and 100 mL was added to the reactor, along with 100 mg photocatalyst to create a 1 g/L catalyst loading. The initial pH of the solution was ~6.5 before starting the photocatalytic reaction. The reaction mixture was stirred in the dark for one hour to allow adsorption equilibrium to be reached before turning on the light. Then, at fixed time intervals, 2 mL of the reaction mixture was drawn and centrifuged at 6000 rpm (Labnet C-1200 Mini Centrifuge) for 4 min. The supernatant was analyzed in triplicate by a UPLC (WATERS Acquity H-class) equipped with an ACQUITY UPLC BEH C18 Column (2.1 mm × 100 mm, 1.7 µm). The concentration of 2,4-DCP was recorded by optical spectrum measurement at 284 nm. The mobile phase in the UPLC consisted of acetonitrile and 0.1% trifluoroacetic acid solution at a flow rate of 0.35 mL/min (25 °C). The total organic carbon (TOC) was determined with a Shimadzu TOC-LCPH/CPN. The reaction for each photocatalyst was repeated three times.

Figure 1. A photograph of the photoreactor setup for the photocatalytic oxidation of the 2,4-DCP.

The 2,4-DCP conversion was calculated according to Equation (2):

$$\text{conversion } (\%) = \frac{C_0 - C_t}{C_0} \times 100 \quad (2)$$

where C_0 and C_t are the initial and final concentrations of the 2,4-DCP and t indicates the reaction time. Meanwhile, the mineralization and energy yield are presented in Equations (3) and (4):

$$\text{mineralization } (\%) = \frac{TOC_0 - TOC_t}{TOC_0} \times 100 \quad (3)$$

where TOC_0 and TOC_t are the initial and final concentrations of the *TOC* at time t, respectively and the energy yield (Y, g/kWh) represents the energy efficiency of the pollutant degradation and is strongly influenced by the reactor design and light source [37]:

$$\text{Y} = \frac{[C_0] \times V \times \eta(\%) \times (1/100)}{P \times t} \quad (4)$$

where C_0 is for the initial concentration of the 2,4-DCP, η is the degradation efficiency (%) at the reaction time t, and P is the nominal power of the light source (kW). G_{50} is the energy yield when the degradation efficiency is 50% (η = 50%) at a reaction time of t_{50}. The related cost is calculated according to the electricity cost in Hong Kong.

3. Results and Discussion

3.1. Fe/TiO$_2$ Photocatalysts

Figure 2 plots the X-ray diffraction of the rutile and ball-milled TiO_2 and the prepared Fe/TiO_2 samples, which display only diffraction peaks corresponding to the rutile TiO_2 [38,39]. Doping the samples with 5 wt.% Fe^{3+} showed a slight 0.033° shift for the Fe/TiO_2-34 and Fe/TiO_2-17, and a 0.066° shift for the Fe/TiO_2-7. In contrast, the ball-milled TiO_2 did not show any diffraction shift from that of the rutile TiO_2. This slight shrinkage in the lattice (i.e., 0.00003 and 0.006 Å, respectively) is consistent with the lattice substitution of Fe^{3+} for Ti^{4+}. Indeed, the Fe^{3+} ion (0.64 Å) is slightly smaller than the Ti^{4+}'s radii (0.68 Å), and i9t can readily be inserted into the TiO_2 lattice [40]. The crystal size was smaller following ball-milling, as indicated by the diffraction peaks broadening, and the ball-milled TiO_2 measured 48.3, 45.1, and 41 nm for the Fe/TiO_2-34, Fe/TiO_2-17, and Fe/TiO_2-7, respectively, compared to the rutile TiO_2 (73.3 nm).

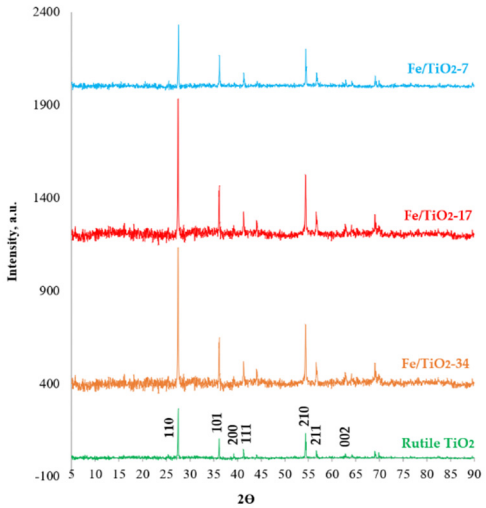

Figure 2. X-ray diffraction patterns of the rutile TiO_2 (Rutile), ball-milled TiO_2 (Rutile-7), and Fe/TiO_2 (B/P = 7, 17, and 34) prepared by mechanochemical ball-milling at 400 rpm for 10 h.

The micro-Raman spectra in Figure 3 are consistent with the XRD data and display only the characteristic bands of the rutile TiO_2 at 144 cm^{-1} (B_{1g}), 449 cm^{-1} (E_g), and 611 cm^{-1} (A_{1g}). The 237 and 1049 cm^{-1} bands originate from multiple phonon-scattering processes and NO_3^- ions, respectively [41,42]. The absence of iron-related bands indicates the successful doping of iron into the TiO_2. In addition, there were no contaminants from the milling bar and jar detected in the samples. The ball-milled Fe/TiO_2 had a light-yellow color compared to the rutile and ball-milled TiO_2, as shown in Figure 4.

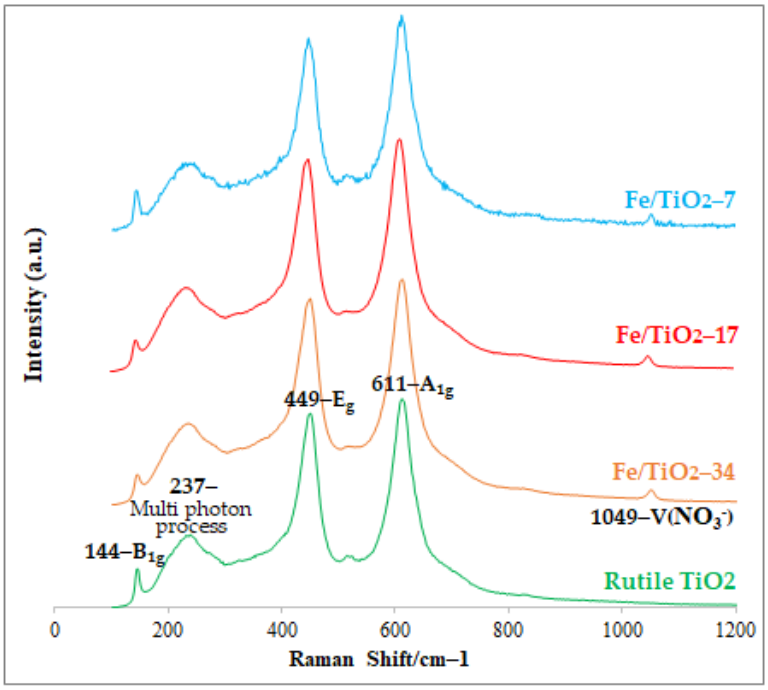

Figure 3. Micro-Raman spectra of the rutile TiO_2 (Rutile), ball-milled TiO_2 (Rutile-7), and Fe/TiO_2 (B/P = 7, 17, and 34) prepared by mechanochemical ball-milling at 400 rpm for 10 h.

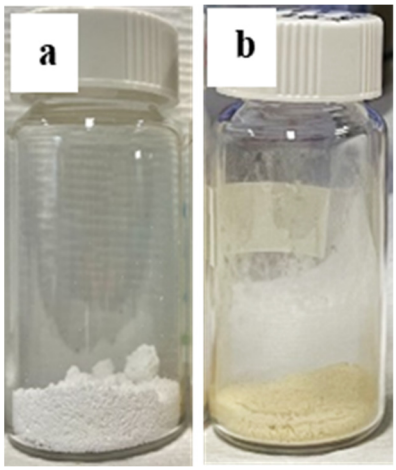

Figure 4. Photographs of (**a**) rutile TiO_2 and (**b**) ball-milled Fe/TiO_2-7.

Figure 5 presents the scanning electron micrographs of the rutile TiO_2 (Figure 5a), Fe/TiO_2-34 (Figure 5b), Fe/TiO_2-17 (Figure 5c), and Fe/TiO_2-7 (Figure 5d). During ball-milling, the sample underwent collisions and attritions which subjected the particles to repetitive breaking–welding–breaking cycles that gradually abraded large particles into fine grains [43]. The ball-milled Fe/TiO_2 samples are less aggregated and better dispersed than the rutile TiO_2 (Figure 5a). Further, the Fe/TiO_2 powders prepared with balls of different

sizes (i.e., 15, 12, 8, and 5 mm) have a broader particle size distribution (cf. Figure 5b,c) compared to the powder ball-milled with balls of similar sizes (i.e., 8 and 5 mm), as shown in Figure 5d. The Fe/TiO_2 milled at a higher B/P with less sample led to air-grinding and rounder particles.

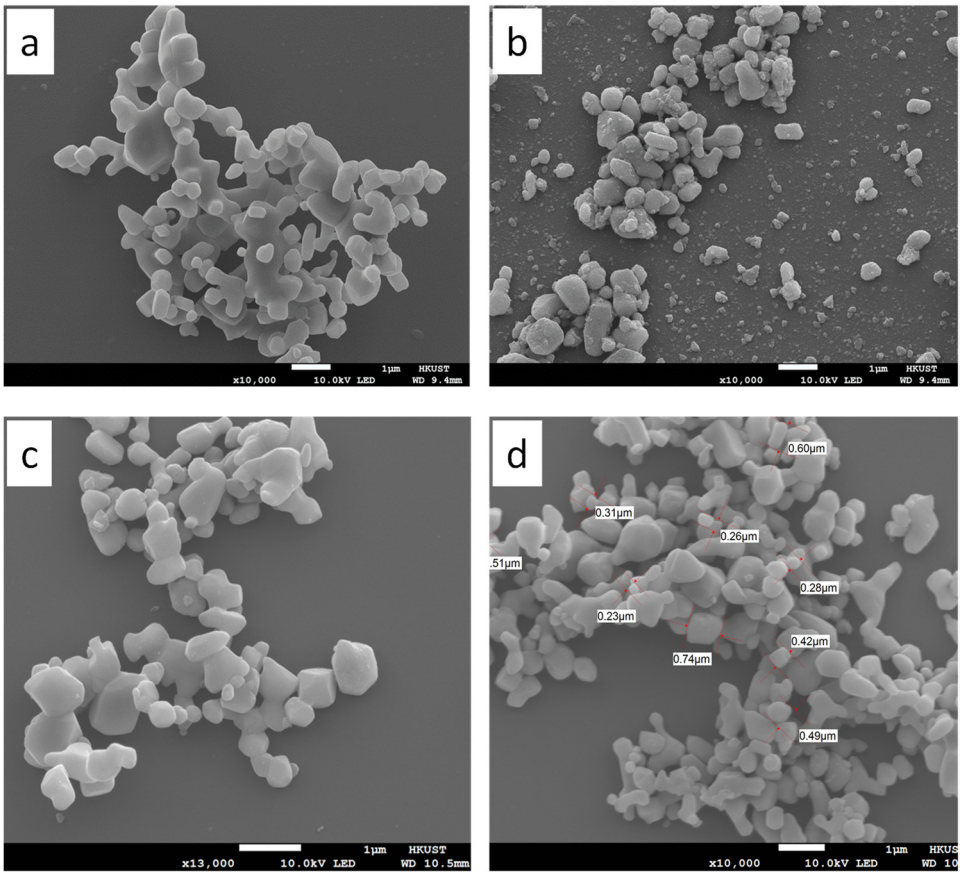

Figure 5. SEM images of (**a**) pristine TiO_2, (**b**) Fe/TiO_2-34, (**c**) Fe/TiO_2-17, and (**d**) Fe/TiO_2-7.

Figure 6 plots the N_2 adsorption–desorption isotherms of the rutile TiO_2 and Fe/TiO_2-7. Both isotherms are type IV curves with hysteresis loops, which are associated with a mesoporous range (2–50 nm, according to IUPAC classification) [44]. Mesopores are known to enhance diffusion, and thus enhance photocatalytic reactions [45], and according to the BJH model, the mean pore diameters of rutile TiO_2 and Fe/TiO_2-7 are 7.39 and 14.83 nm, respectively. Table 1 shows the B/P decreasing from 34 to 7, resulting in a smaller mean pore diameter (52.41 to 16.20 and 14.83 nm).

The UV-Vis diffuse reflectance spectra (DRS) and corresponding Tauc plots of the rutile TiO_2 and Fe/TiO_2-7 are presented in Figure 7. The TiO_2 has an absorption edge at the 368 nm wavelength (Figure 7a) and calculated bandgap energy (E_g) of 3.00 eV (at the 417 nm cut-off Landa), which is consistent with the literature [46,47]. Ball-milled Fe/TiO_2 shifts the absorption edge of the visible region (546 nm) and narrows the bandgap to 2.22 eV. It is believed the iron creates new e^-/h^+ and traps energy levels (Fe^{4+}/Fe^{3+} and Fe^{3+}/Fe^{2+}) between the conduction band and valence band of TiO_2 precursors [48,49]. Lattice defects from ball-milling can also play a role [50]. The earlier work by Carneiro et al. [50] prepared Fe/TiO_2 by ball-milling aeroxide TiO_2 P25 with 10 wt.% Fe to obtain photocatalysts that were 2.45 eV broader, in comparison with this study.

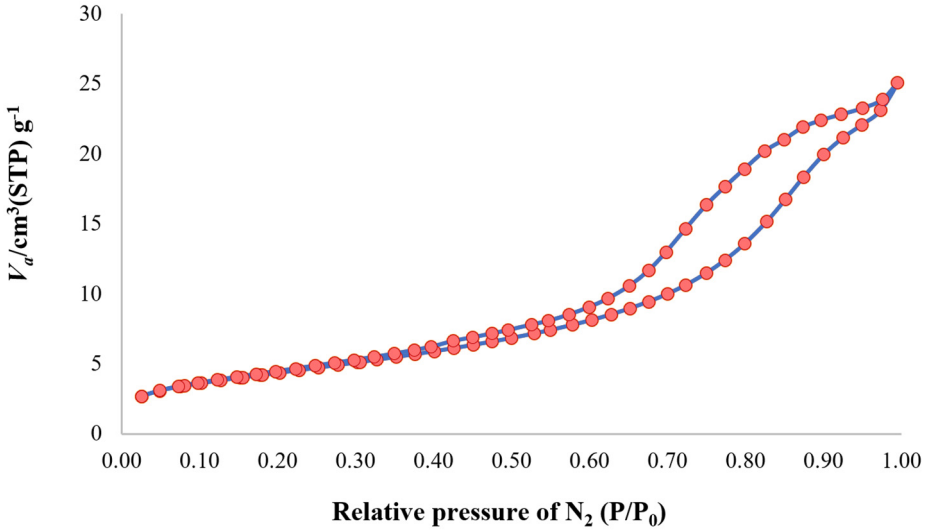

Figure 6. Nitrogen physisorption isotherms for ball-milled Fe/TiO_2-7.

Table 1. Surface properties of the rutile TiO_2 and produced Fe/TiO_2 catalysts.

Catalysts	BET Surface Area (m^2 g^{-1})	Average Pore Diameter (nm)	Total Pore Volume (cm^3 g^{-1})	Crystal Size (nm)
Rutile TiO_2	2.69	7.39	0.013	73.3
Fe/TiO_2-34	5.78	52.41	0.023	48.3
Fe/TiO_2-17	6.46	16.20	0.028	45.1
Fe/TiO_2-7	6.87	14.83	0.071	41

Figure 8 compares the electronic structure of the rutile TiO_2 and Fe/TiO_2-7. According to XPS measurements, the conduction band of Fe/TiO_2-7 is 0.67 eV compared to 0 eV for the rutile TiO_2 and the valence band is 2.89 eV against TiO_2's 3.00 eV. Electrons and holes are generated by the photocatalyst as it absorbs photons with energy equal to or greater than its bandgap energy. The electrons and holes migrate to the catalyst surface and react with adsorbed O_2 or H_2O to generate reactive hydroxyl radicals ($^{\bullet}OH$), superoxide radicals ($O_2^{\bullet-}$), and holes (h^+) that oxidize the pollutants to reactive intermediates. The highly reactive $^{\bullet}OH$ (redox potential = +3.06 V) is generated by water decomposition or holes and an ^{-}OH reaction, while the superoxide anion ($O_2^{\bullet-}$) can participate in the production of a hydroperoxyl radical ($HO_2^{\bullet}$) and, subsequently, H_2O_2. The general mechanism of photocatalysis over TiO_2 is summarized in Equations (5)–(19) [51–55], as follows:

$$\text{Light irradiation and photoexcitation: } TiO_2 + h\nu \rightarrow e^- + h^+ \quad (5)$$

$$e^- \text{ trapping: } e^-_{CB} \rightarrow e^-_{TR} \quad (6)$$

$$h^+ \text{ trapping: } h^+_{VB} \rightarrow h^+_{TR} \quad (7)$$

$$h^+ + H_2O \rightarrow {}^{\bullet}OH + H^+ \quad (8)$$

$$\text{Hydroxyl oxidation: } OH^- + h^+ \rightarrow {}^{\bullet}OH \quad (9)$$

$$h^+ + 2H_2O \rightarrow H_2O_2 + H^+ \quad (10)$$

$$e^- \text{ scavenging: } (O_2)_{ads} + e^- \rightarrow O_2^{\bullet-} \quad (11)$$

$$\text{Superoxide protonation: } O_2^{\bullet-} + H^+ \rightarrow HO_2^{\bullet} \quad (12)$$

$$e^- \text{ co-scavenging: } HO_2^{\bullet} + e^- \rightarrow HO_2^- \quad (13)$$

$$H_2O_2 \text{ formation: } e^- + O_2^{\bullet-} + 2H^+ \rightarrow H_2O_2 \quad (14)$$

$$e^- + H_2O_2 \rightarrow {}^{\bullet}OH + OH^- \quad (15)$$

$$O_2^{\bullet -} + H_2O_2 \rightarrow {}^{\bullet}OH + OH^- + O_2 \quad (16)$$

$$2HO_2^{\bullet} \rightarrow O_2 + H_2O_2 \quad (17)$$

$$\text{Photocatalytic oxidation by } {}^{\bullet}OH\text{: R-H} + {}^{\bullet}OH \rightarrow R^{\bullet} + H_2O \quad (18)$$

$$\text{Photocatalytic oxidation by direct } h^+\text{: R-H} + h^+ \rightarrow {}^{\bullet}R^+ \rightarrow \text{degradation by-products} \quad (19)$$

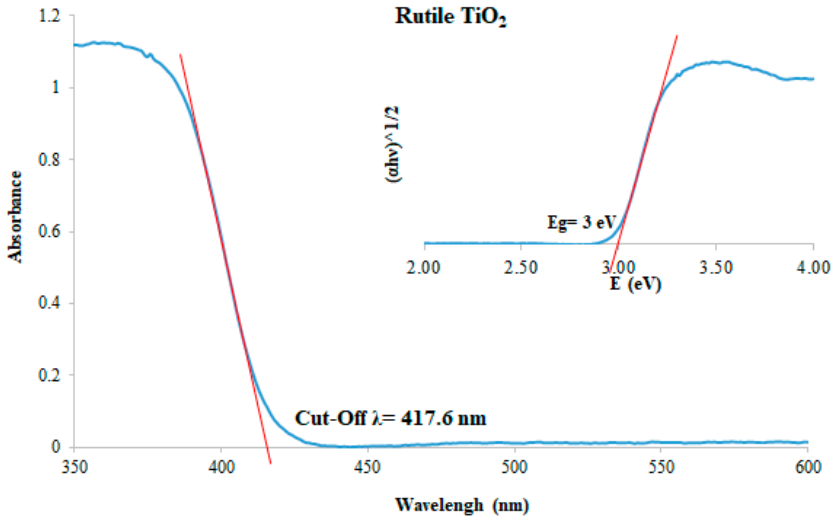

(**a**)

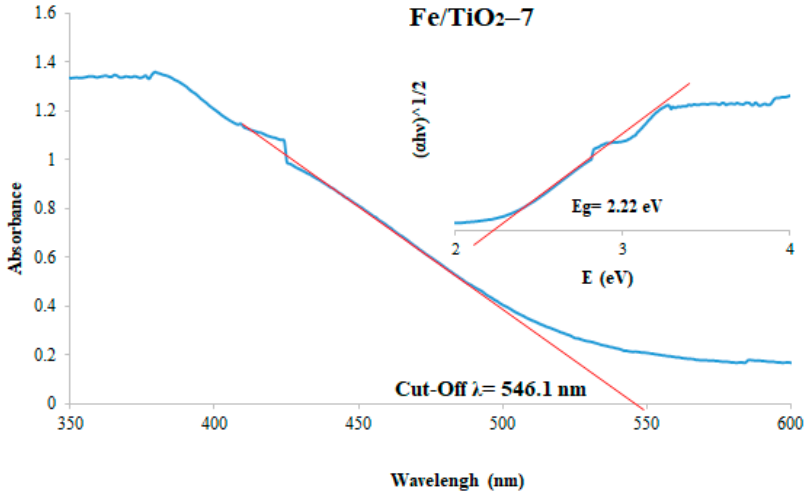

(**b**)

Figure 7. UV-Vis diffuse reflectance spectra of the (**a**) bare rutile TiO_2 and (**b**) Fe/TiO_2-7, with their corresponding Tauc plot insets.

The XPS analysis of the rutile TiO_2 and Fe/TiO_2-7 is shown in Figure 9. The O 1s peak at 530.1 eV (Figure 9a) belongs to the lattice oxygen [56], and the peak at 532.8 eV is from chemisorbed (O) [56]. The Ti 2p spectra in Figure 9b show two main peaks of $Ti2p_{3/2}$ and $Ti2p_{1/2}$ at 458.8 and 464.6 eV, respectively, with a signal separation of 5.8 eV, which corresponds to Ti^{4+} [57,58]. Compared to the rutile TiO_2, the Ti $2p_{3/2}$ and Ti $2p_{1/2}$ peaks shifted upward by 0.3 eV, which is attributed to lattice distortions following Fe^{3+} doping and the milling process. Figure 9c displays two peaks at 725 and 711.3 eV, assigned to Fe $2p_{1/2}$ and Fe $2p_{3/2}$, respectively. A satellite peak at 719.2 eV indicates the presence of Fe^{3+} [59]. All these peaks provide conclusive evidence for the presence of Fe^{3+} ions in the samples [56,60]. None of the binding energies of the Fe^{2+} (709 and 723 eV) and zero-valent

iron (707 and 720 eV) were observed [61,62], which indicates the successful insertion of iron into the TiO_2 lattice.

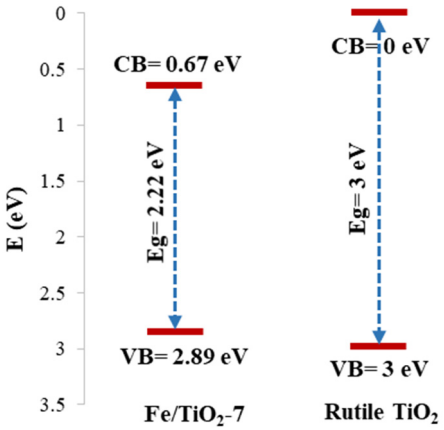

Figure 8. Electronic structure of the rutile TiO_2 and Fe/TiO_2-7 from UV-Vis DRS and XPS measurements.

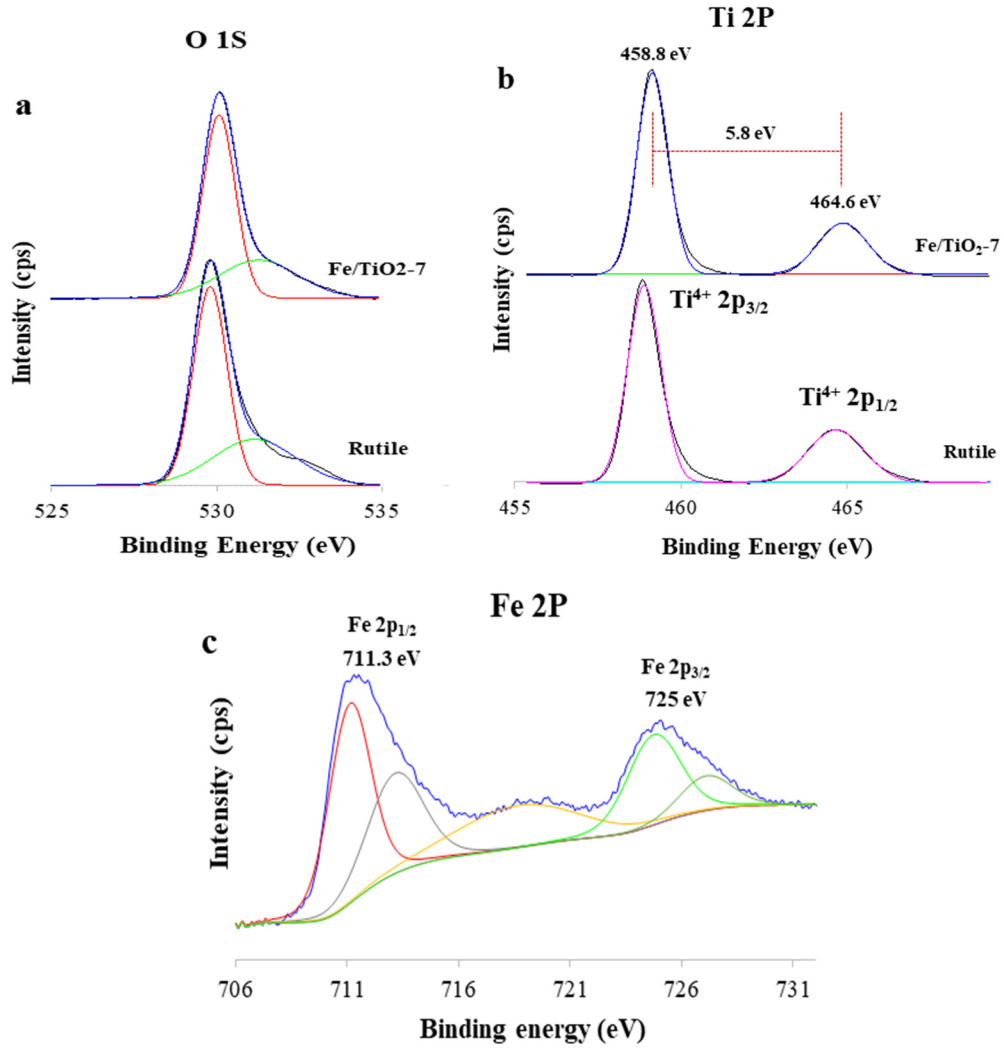

Figure 9. Deconvolution and XPS spectra curve fitting for the (**a**) O 1 s, (**b**) Ti 2p, and (**c**) Fe 2p of TiO_2 and Fe/TiO_2-7.

3.2. Photocatalytic Oxidation of the 2,4-DCP

Figure 10 presents the photocatalytic oxidation of the 2,4-DCP over the rutile TiO_2 and ball-milled Fe/TiO_2 photocatalysts. After equilibrating under dark conditions, the 0.1 g TiO_2, Fe/TiO_2-34, Fe/TiO_2-17, and Fe/TiO_2-7 photocatalysts adsorbed 16.8, 18.8, 26.7, and 19.7%, respectively, of 4.08 mg/L 2,4-DCP (100 mL) and converted 59.4, 64.4, 71.8, and 81.4%, respectively, of 2,4-DCP after 24 h irradiation under visible light. A photolysis experiment exhibited a negligible reduction in the 2,4-DCP concentration (7.5%) after 24 h. The Fe/TiO_2 is a more efficient photocatalyst, as Fe^{3+} ions can transform into Fe^{2+} and Fe^{4+} ions trapping e^-/h^+, as described in Equations (20) and (21) [63]:

$$Fe^{3+} + h^+ \rightarrow Fe^{4+} \quad (20)$$

$$Fe^{3+} + e^- \rightarrow Fe^{2+} \quad (21)$$

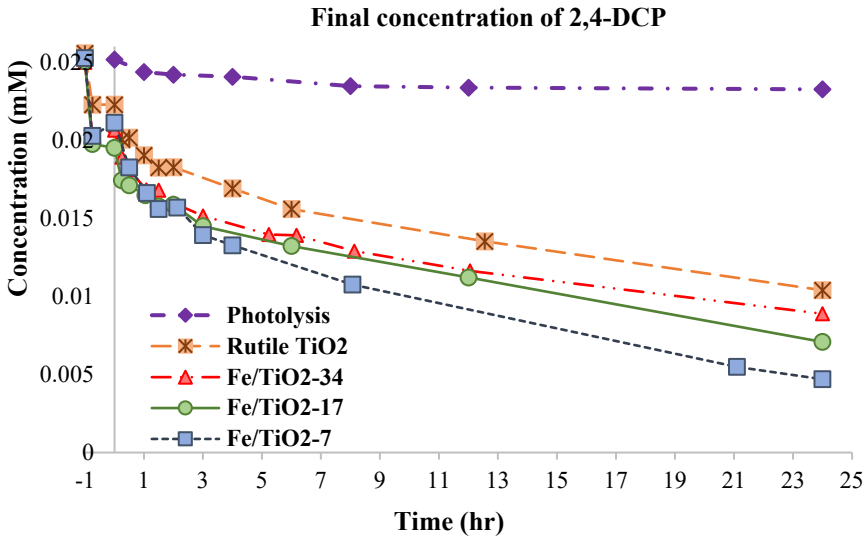

Figure 10. Plots of the 2,4–DCP concentrations during photocatalytic oxidation reactions over the rutile TiO_2, Fe/TiO_2-34, Fe/TiO_2-17, and Fe/TiO_2-7 under visible light irradiation. Note: $[2,4\text{–DCP}]_0$ = 4.08 mg/L, $[TOC]_0$ = 9.47 mg/L, catalyst loading = 1 g/L, room temperature, no pH adjustment.

The Fe^{2+} and Fe^{4+}, being less stable than Fe^{3+} and their relative energy levels Fe^{3+}/Fe^{4+} and Fe^{3+}/Fe^{2+} (Figure 11), allow the trapping of photo-generated e^-/h^+ and increase their lifetimes [64]. Prior work [65] has indicated that the energy level of the Fe^{3+}/Fe^{2+} is below the TiO_2 conduction band, while that of Fe^{4+}/Fe^{3+} is above the TiO_2 valence band [66]. Therefore, the transition of e^- from Fe 3d orbitals to CB of TiO_2 induces local states below the conduction band edge. This can significantly decrease the bandgap and increase the removal efficiency [59,66].

Figure 12 presents the photoreaction kinetics, assuming a Langmuir–Hinshelwood (LH)) model as described by Equation (22) [67]:

$$r = -\frac{dC}{dT} = \frac{k_{LH} \times K \times C_t}{1 + K \times C_t} \quad (22)$$

where r, C_t, t, k_{LH}, and K refer to the reaction rate (mg/L·h), the concentration of 2,4-DCP at the reaction time t (mg/L), reaction time (h), photocatalytic reaction rate constant (h^{-1}), and equilibrium constant for adsorption (L/mg), respectively. In heterogeneous photocatalytic reactions and at low concentrations ($K \times C_t << 1$), Equation (22) can be simplified to Equation (23) [68]:

$$r = -\frac{dC}{dT} = k_{app} \times C \quad (23)$$

where k_{app} is the apparent rate constant and can be calculated by plotting the graph of $\ln(C_t)$ versus t, as shown in Figure 12. Table 2 summarizes the reaction rate constant (k) and the linear correlation coefficients (R^2) for the rutile TiO_2 and Fe/TiO_2 photocatalysts.

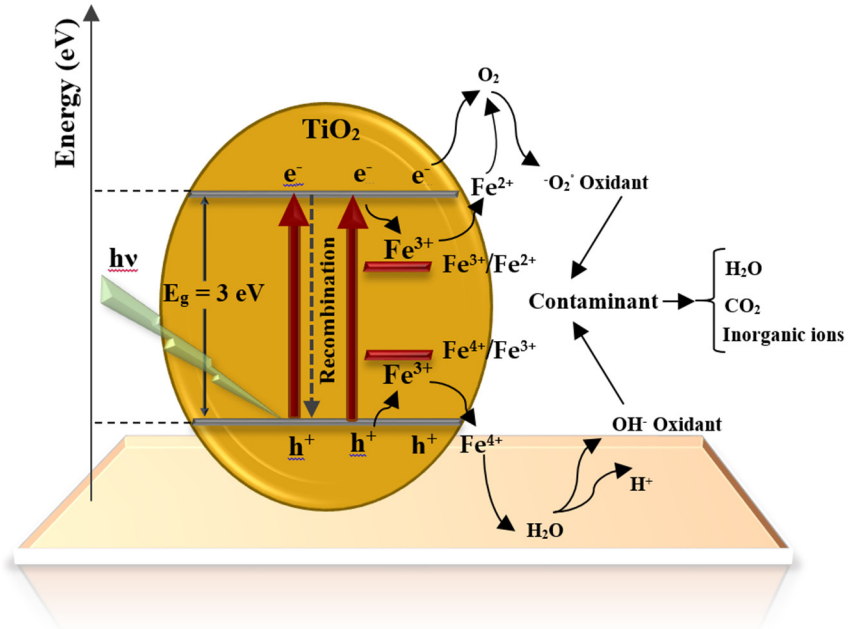

Figure 11. Schematic display of the electronic band structure of Fe/TiO_2-7.

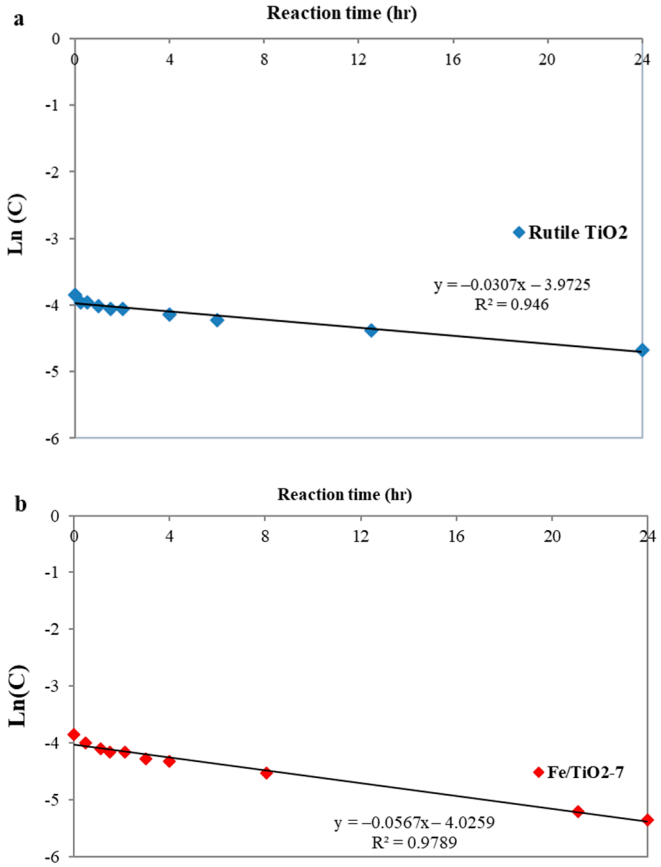

Figure 12. Linear-log plot $\ln(C_0)$ versus reaction time (h) for the degradation kinetic after 24 h reaction using (**a**) rutile and (**b**) Fe/TiO_2-7 photocatalysts.

Table 2. Kinetic parameters of the Fe/TiO_2 samples (C_0 = 0.025 mM, catalyst = 1 g/L).

Samples	Reaction Rate Constant (k, h^{-1})	Correlation Coefficient (R^2)	Removal Efficiency (%)
Rutile TiO_2	0.031	0.95	59.4
Fe/TiO_2-34	0.032	0.91	64.4
Fe/TiO_2-17	0.035	0.96	71.8
Fe/TiO_2-7	0.057	0.98	81.4

Among the catalysts, Fe/TiO_2-7 indicated the best performance in 2,4-DCP conversion. Despite using low-power light in the present study, the result is favorably comparable to the photocatalytic yield of Fe/TiO_2 photocatalysts reported in other studies. The 10 wt.% Fe/TiO_2 ball-milled catalyst (B/P = 8, 250 rpm, 5 h) prepared by Carneiro et al. [50] degraded 50.7% rhodamine B (5 mg/L) after 2 h irradiation under a pair of 15 W UV lamps. The 5 wt.% Fe/TiO_2 (B/P = 5, 300 rpm, 5 h) prepared by Hadi et al. [69] converted 37% methylene blue (2 mg/L) after 4 h irradiation under 150 W visible light. Ramírez-Sánchez and Bandala [45] fabricated a hydrothermal sol-gel Fe/TiO_2 catalyst which converted 10.63% estriol (2.9 mg/L) within 8 h of irradiation under a pair of 15 W visible light lamps (without UV cut-off filters). Mancuso et al. [63] prepared 3.5 wt.% Fe/TiO_2 via a soft-templating method for treating 10 mg/L Acid Orange 7. They reported 32% conversion after a 3 h reaction time under 10 W white LED lighting.

Figure 13 plots the TOC with the reaction time for the rutile TiO_2 and Fe/TiO_2-7, showing that the latter has a greater mineralization of 2,4-DCP pollutants (i.e., 63.5 vs. 49.4%). In comparison, the 1 wt.% Fe/TiO_2 prepared by the $NaBH_4$ reduction method [70] reached 35% TOC removal for a 2,4-DCP solution after 3 h under an intense 100 W tungsten halogen lamp and vigorous aeration. Slow mineralization indicates the presence of refractory by-products that can pose more hazards than the main contaminant [71].

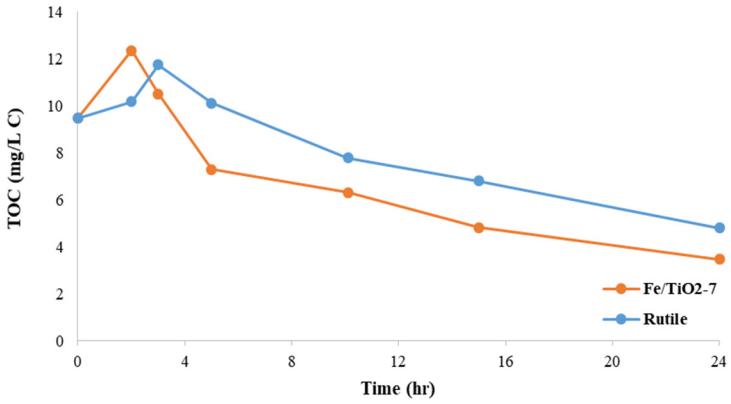

Figure 13. Plots of TOC removal during photocatalytic oxidation reactions over TiO_2 and Fe/TiO_2-7 under visible light irradiation. Note: $[2,4\text{-DCP}]_0$ = 4.08 mg/L, $[TOC]_0$ = 9.47 mg/L, catalyst loading = 1 g/L, room temperature, no pH adjustment.

The energy consumed during the photocatalytic reaction is essential for calculating the operating cost of pollution treatment [72]. The G50s for the decomposition of 4.08 mg/L 2,4-DCP in the laboratory photoreactor setup using the rutile TiO_2 and Fe/TiO_2-7 were 0.13 and 0.06 g 2,4-DCP/kW·h. Thus, the Fe/TiO_2-7's energy yield is approximately twice that of the rutile TiO_2. It costs $0.077 and $0.168 to degrade a gram of 2,4-DCP, according to Hong Kong electricity costs [73].

4. Conclusions

Ball-milling allows a simple and inexpensive method for inserting iron dopants into TiO_2 to produce a series of visible light, photoactive Fe/TiO_2 catalysts that include 5 wt.% iron. It is a green synthesis method that avoids the use of solvents. Applying different B/P

ratios (34, 17, 7) and differently sized balls affect the particle morphology and size distribution. The mesoporous Fe/TiO_2-7 prepared under optimum milling conditions (B/p: 7, at 400 rpm and 10 h) displayed the best photocatalytic activity. Fe^{3+} was successfully inserted into the TiO_2 lattice, with no extraneous iron detected by XPS or micro-Raman. A concomitant change in lattice spacing was detected by XRD following the preparation of the Fe/TiO_2-7. It was two times more efficient at 2,4-DCP conversion and mineralization compared to the rutile TiO_2 and the other catalysts. The catalyst's performance is commensurate to, or better than, similar Fe/TiO_2 photocatalysts and requires less energy to degrade pollutants ($0.077 with respect to Hong Kong electricity costs).

Author Contributions: S.T.: methodology, investigation, software, writing—review and editing. K.-L.Y.: supervision, writing—review and editing, funding acquisition, and resources. B.A.-A.: supervision and review. All authors have read and agreed to the published version of the manuscript.

Funding: The authors are grateful for the financial support from the Hong Kong Research Grant Council (16211421), the Project of Hetao Shenzhen-Hong Kong Science and Technology Innovation Cooperation Zone (HZQB-KCZYB-2020083), and the staff from the MCPF, AEMF, and CBE in HKUST.

Institutional Review Board Statement: Not applicable.

Informed Consent Statement: Not applicable.

Data Availability Statement: Not applicable.

Acknowledgments: The authors acknowledge the funding of Postgraduate Studentships (PGSs) awarded by the Hong Kong University of Science and Technology.

Conflicts of Interest: The authors declare no competing financial interests.

References

1. Naseri, A.; Sarabi, G.A.; Samadi, M.; Yousefi, M.; Ebrahimi, M.; Moshfegh, A.Z. Recent advances on dual-functional photocatalytic systems for combined removal of hazardous water pollutants and energy generation. *Res. Chem. Intermed.* **2022**, *48*, 911–933. [CrossRef]
2. Boretti, A.; Rosa, L. Reassessing the projections of the World Water Development Report. *npj Clean Water* **2019**, *2*, 15. [CrossRef]
3. Mariana, M.; HPS, A.K.; Yahya, E.B.; Olaiya, N.; Alfatah, T.; Suriani, A.; Mohamed, A. Recent trends and future prospects of nanostructured aerogels in water treatment applications. *J. Water Process Eng.* **2021**, *45*, 102481. [CrossRef]
4. Hojjati-Najafabadi, A.; Mansoorianfar, M.; Liang, T.; Shahin, K.; Karimi-Maleh, H. A review on magnetic sensors for monitoring of hazardous pollutants in water resources. *Sci. Total Environ.* **2022**, *824*, 153844. [CrossRef]
5. Kadmi, Y.; Favier, L.; Yehya, T.; Soutrel, I.; Simion, A.I.; Vial, C.; Wolbert, D. Controlling contamination for determination of ultra-trace levels of priority pollutants chlorophenols in environmental water matrices. *Arab. J. Chem.* **2019**, *12*, 2905–2913. [CrossRef]
6. Zhu, X.; Zhang, K.; Wang, C.; Guan, J.; Yuan, X.; Li, B. Quantitative determination and toxicity evaluation of 2, 4-dichlorophenol using poly (eosin Y)/hydroxylated multi-walled carbon nanotubes modified electrode. *Sci. Rep.* **2016**, *6*, 1–12. [CrossRef]
7. Esmaeili, N.; Saraei, F.E.K.; Pirbazari, A.E.; Tabatabai-Yazdi, F.-S.; Khodaee, Z.; Amirinezhad, A.; Esmaeili, A.; Pirbazari, A.E. Estimation of 2,4-dichlorophenol photocatalytic removal using different artificial intelligence approaches. *Chem. Prod. Process Model.* **2021**. [CrossRef]
8. Wu, C.; Zhou, L.; Zhou, C.; Zhou, Y.; Zhou, J.; Xia, S.; Rittmann, B.E. A kinetic model for 2,4-dichlorophenol adsorption and hydrodechlorination over a palladized biofilm. *Water Res.* **2022**, *214*, 118201. [CrossRef]
9. Marwat, M.A.; Ullah, H.; Usman, M.; Ehsan, M.A.; Zhang, H.; Khan, M.F.; Ali, S.; Yousaf, M. Significantly improved photocatalytic activity of the SnO2/BiFeO3 heterojunction for pollutant degradation and mechanism. *Ceram. Int.* **2022**, *48*, 14789–14798. [CrossRef]
10. Taghipour, S.; Ayati, B. Cultivation of aerobic granules through synthetic petroleum wastewater treatment in a cyclic aerobic granular reactor. *Desalination Water Treat.* **2017**, *76*, 134–142. [CrossRef]
11. Taghipour, S.; Ayati, B.; Razaei, M. Study of the SBAR performance in COD removal of Petroleum and MTBE. *Modares Civ. Eng. J.* **2017**, *17*, 17–27.
12. Taghipour, S.; Ayati, B. Study of SBAR Capability in Petroleum Wastewater Treatment. *Water Reuse* **2015**, *2*, 119–128.
13. Taghipour, S.; Jannesari, M.; Ataie-Ashtiani, B.; Hosseini, S.M.; Taghipour, M. Catalytic Processes for Removal of Emerging Water Pollutants. In *Emerging Water Pollutants: Concerns and Remediation Technologies*; Bentham Science: Sharjah, United Arab Emirates, 2022; Volume 1, pp. 290–325. [CrossRef]
14. Khorsandi, H.; Teymori, M.; Aghapour, A.A.; Jafari, S.J.; Taghipour, S.; Bargeshadi, R. Photodegradation of ceftriaxone in aqueous solution by using UVC and UVC/H2O2 oxidation processes. *Appl. Water Sci.* **2019**, *9*, 81. [CrossRef]

15. Wang, Z.; Xu, J.; Yang, J.; Xue, Y.; Dai, L. Ultraviolet/ozone treatment for boosting OER activity of MOF nanoneedle arrays. *Chem. Eng. J.* **2021**, *427*, 131498. [CrossRef]
16. Gomes, J.; Bernardo, C.; Jesus, F.; Pereira, J.L.; Martins, R.C. Ozone Kinetic Studies Assessment for the PPCPs Abatement: Mixtures Relevance. *ChemEngineering* **2022**, *6*, 20. [CrossRef]
17. Pandis, P.K.; Kalogirou, C.; Kanellou, E.; Vaitsis, C.; Savvidou, M.G.; Sourkouni, G.; Zorpas, A.A.; Argirusis, C. Key Points of Advanced Oxidation Processes (AOPs) for Wastewater, Organic Pollutants and Pharmaceutical Waste Treatment: A Mini Review. *ChemEngineering* **2022**, *6*, 8. [CrossRef]
18. Jabbar, Z.H.; Ebrahim, S.E. Recent advances in nano-semiconductors photocatalysis for degrading organic contaminants and microbial disinfection in wastewater: A comprehensive review. *Environ. Nanotechnol. Monit. Manag.* **2022**, *17*, 100666. [CrossRef]
19. Taghipour, S.; Khadir, A.; Taghipour, M. Carbon Nanotubes Composite Membrane for Water Desalination. In *Sustainable Materials and Systems for Water Desalination*; Springer: Cham, Switzerland, 2021; pp. 163–184.
20. Khadir, A.; Ramezanali, A.M.; Taghipour, S.; Jafari, K. Insights of the Removal of Antibiotics from Water and Wastewater: A Review on Physical, Chemical, and Biological Techniques. In *Applied Water Science: Remediation Technologies*; Wiley: Hoboken, NJ, USA, 2021; Volume 2, pp. 1–47.
21. Li, Z.; Li, Z.; Zuo, C.; Fang, X. Application of Nanostructured TiO2 in UV Photodetectors: A Review. *Adv. Mater.* **2022**, *2*, 2109083. [CrossRef]
22. Su, K.; Li, L.; Deng, S.; Gao, Z.; Qin, Q.; Yang, J.; Zhang, S.; Chen, J. Research progress of TiO_2 photocatalytic reduction of oxyanion pollutants in water: A mini review. *Green Chem. Lett. Rev.* **2021**, *15*, 35–44. [CrossRef]
23. Algarin, P.C. Effects of Zn Doping and High Energy Ball Milling on the Photocatalytic Properties of TiO2. Master's Thesis, University of South Florida, Tampa, FL, USA, 2008.
24. Wu, D.; Li, C.; Zhang, D.; Wang, L.; Zhang, X.; Shi, Z.; Lin, Q. Enhanced photocatalytic activity of Gd3+ doped TiO2 and Gd2O3 modified TiO2 prepared via ball milling method. *J. Rare Earths* **2019**, *37*, 845–852. [CrossRef]
25. Saber, D.; El-Aziz, K.; Felemban, B.F.; Alghtani, A.H.; Ali, H.T.; Ahmed, E.M.; Megahed, M. Characterization and performance evaluation of Cu-based/TiO2 nano composites. *Sci. Rep.* **2022**, *12*, 1–14. [CrossRef] [PubMed]
26. Wu, D.; Li, C.; Kong, Q.; Shi, Z.; Zhang, D.; Wang, L.; Han, L.; Zhang, X.; Lin, Q. Photocatalytic activity of Lu3+/TiO2 prepared by ball milling method. *J. Rare Earths* **2018**, *36*, 819–825. [CrossRef]
27. Santos, D.M.D.L.; Navas, J.; Sánchez-Coronilla, A.; Alcántara, R.; Fernández-Lorenzo, C.; Martín-Calleja, J. Highly Al-doped TiO2 nanoparticles produced by Ball Mill Method: Structural and electronic characterization. *Mater. Res. Bull.* **2015**, *70*, 704–711. [CrossRef]
28. Nasralla, N.; Yeganeh, M.; Astuti, Y.; Piticharoenphun, S.; Shahtahmasebi, N.; Kompany, A.; Karimipour, M.; Mendis, B.G.; Poolton, N.R.J.; Šiller, L. Structural and spectroscopic study of Fe-doped TiO2 nanoparticles prepared by sol–gel method. *Sci. Iran.* **2013**, *20*, 1018–1022.
29. Kissoum, Y.; Mekki, D.E.; Bououdina, M.; Sakher, E.; Bellucci, S. Dependence of Fe Doping and Milling on TiO2 Phase Transformation: Optical and Magnetic Studies. *J. Supercond. Nov. Magn.* **2019**, *33*, 427–440. [CrossRef]
30. Wei, M.; Wang, B.; Chen, M.; Lyu, H.; Lee, X.; Wang, S.; Yu, Z.; Zhang, X. Recent advances in the treatment of contaminated soils by ball milling technology: Classification, mechanisms, and applications. *J. Clean. Prod.* **2022**, *340*, 130821. [CrossRef]
31. Kumar, M.; Xiong, X.; Wan, Z.; Sun, Y.; Tsang, D.C.; Gupta, J.; Gao, B.; Cao, X.; Tang, J.; Ok, Y.S. Ball milling as a mechanochemical technology for fabrication of novel biochar nanomaterials. *Bioresour. Technol.* **2020**, *312*, 123613. [CrossRef] [PubMed]
32. Krusenbaum, A.; Grätz, S.; Tigineh, G.T.; Borchardt, L.; Kim, J.G. The mechanochemical synthesis of polymers. *Chem. Soc. Rev.* **2022**, *51*, 2873–2905. [CrossRef]
33. Coste, S.; Bertrand, G.; Coddet, C.; Gaffet, E.; Hahn, H.; Sieger, H. High-energy ball milling of Al2O3–TiO2 powders. *J. Alloy. Compd.* **2007**, *434–435*, 489–492. [CrossRef]
34. Pedrayes, F.; Norniella, J.G.; Melero, M.G.; Menéndez-Aguado, J.M.; del Coz-Díaz, J.J. Frequency domain characterization of torque in tumbling ball mills using DEM modelling: Application to filling level monitoring. *Powder Technol.* **2018**, *323*, 433–444. [CrossRef]
35. Patterson, A.L. The Scherrer Formula for X-Ray Particle Size Determination. *Phys. Rev.* **1939**, *56*, 978–982. [CrossRef]
36. Paul, T.C.; Podder, J. Synthesis and characterization of Zn-incorporated TiO2 thin films: Impact of crystallite size on X-ray line broadening and bandgap tuning. *Appl. Phys. A* **2019**, *125*, 818. [CrossRef]
37. Wu, L.; Xie, Q.; Lv, Y.; Zhang, Z.; Wu, Z.; Liang, X.; Lu, M.; Nie, Y. Degradation of methylene blue by dielectric barrier discharge plasma coupled with activated carbon supported on polyurethane foam. *RSC Adv.* **2019**, *9*, 25967–25975. [CrossRef] [PubMed]
38. Soundarrajan, P.; Sankarasubramanian, K.; Logu, T.; Sethuraman, K.; Ramamurthi, K. Growth of rutile TiO2 nanorods on TiO2 seed layer prepared using facile low cost chemical methods. *Mater. Lett.* **2014**, *116*, 191–194. [CrossRef]
39. He, J.; Du, Y.-E.; Bai, Y.; An, J.; Cai, X.; Chen, Y.; Wang, P.; Yang, X.; Feng, Q. Facile Formation of Anatase/Rutile TiO2 Nanocomposites with Enhanced Photocatalytic Activity. *Molecules* **2019**, *24*, 2996. [CrossRef]
40. Wan, L.; Chua, D.H.; Sun, H.; Chen, L.; Wang, K.; Lu, T.; Pan, L. Construction of two-dimensional bimetal (Fe-Ti) oxide/carbon/MXene architecture from titanium carbide MXene for ultrahigh-rate lithium-ion storage. *J. Colloid Interface Sci.* **2020**, *588*, 147–156. [CrossRef]
41. Challagulla, S.; Tarafder, K.; Ganesan, R.; Roy, S. Structure sensitive photocatalytic reduction of nitroarenes over TiO 2. *Sci. Rep.* **2017**, *7*, 1–11. [CrossRef]

42. Franceschini, F.; Bartoli, M.; Tagliaferro, A.; Carrara, S. Electrodes for Paracetamol Sensing Modified with Bismuth Oxide and Oxynitrate Heterostructures: An Experimental and Computational Study. *Chemosensors* **2021**, *9*, 361. [CrossRef]
43. Wang, M.; Zhao, Q.; Yang, H.; Shi, D.; Qian, J. Photocatalytic antibacterial properties of copper doped TiO2 prepared by high-energy ball milling. *Ceram. Int.* **2020**, *46*, 16716–16724. [CrossRef]
44. Thommes, M.; Kaneko, K.; Neimark, A.V.; Olivier, J.P.; Rodriguez-Reinoso, F.; Rouquerol, J.; Sing, K.S.W. Physisorption of gases, with special reference to the evaluation of surface area and pore size distribution (IUPAC Technical Report). *Pure Appl. Chem.* **2015**, *87*, 1051–1069. [CrossRef]
45. Ramírez-Sánchez, I.M.; Bandala, E.R. Photocatalytic Degradation of Estriol Using Iron-Doped TiO2 under High and Low UV Irradiation. *Catalysts* **2018**, *8*, 625. [CrossRef]
46. Maleki-Ghaleh, H.; Shakeri, M.; Dargahi, Z.; Kavanlouei, M.; Garabagh, H.K.; Moradpur-Tari, E.; Yourdkhani, A.; Fallah, A.; Zarrabi, A.; Koc, B.; et al. Characterization and optical properties of mechanochemically synthesized molybdenum-doped rutile nanoparticles and their electronic structure studies by density functional theory. *Mater. Today Chem.* **2022**, *24*, 100820. [CrossRef]
47. Luan, P.; Xie, M.; Liu, D.; Fu, X.; Jing, L. Effective charge separation in the rutile TiO2 nanorod-coupled α-Fe2O3 with exceptionally high visible activities. *Sci. Rep.* **2014**, *4*, 6180. [CrossRef] [PubMed]
48. Kanjana, N.; Maiaugree, W.; Laokul, P. Photocatalytic activity of nanocrystalline Fe3+-doped anatase TiO2 hollow spheres in a methylene blue solution under visible-light irradiation. *J. Mater. Sci. Mater. Electron.* **2022**, *33*, 4659–4680. [CrossRef]
49. Moradi, H.; Eshaghi, A.; Hosseini, S.R.; Ghani, K. Fabrication of Fe-doped TiO2 nanoparticles and investigation of photocatalytic decolorization of reactive red 198 under visible light irradiation. *Ultrason. Sonochemistry* **2016**, *32*, 314–319. [CrossRef]
50. Carneiro, J.A.O.; De Azevedo, S.S.; Fernandes, F.D.P.; Freitas, E.; Pereira, M.A.C.D.C.; Tavares, C.J.; Lanceros-Mendez, S.; Teixeira, V.M.P. Synthesis of iron-doped TiO2 nanoparticles by ball-milling process: The influence of process parameters on the structural, optical, magnetic, and photocatalytic properties. *J. Mater. Sci.* **2014**, *49*, 7476–7488. [CrossRef]
51. Taghipour, S.; Hosseini, S.M.; Ataie-Ashtiani, B. Engineering nanomaterials for water and wastewater treatment: Review of classifications, properties and applications. *New J. Chem.* **2019**, *43*, 7902–7927. [CrossRef]
52. Taghipour, S.; Ataie-Ashtiani, B.; Hosseini, S.M.; Yeung, K.L. Graphitic carbon nitride-based composites for photocatalytic abatement of emerging pollutants. In *Micro and Nano Technologies*; Wiley: Hoboken, NJ, USA, 2022; pp. 175–214.
53. Jannesari, M.; Akhavan, O.; Hosseini, H.R.M. Graphene oxide in generation of nanobubbles using controllable microvortices of jet flows. *Carbon* **2018**, *138*, 8–17. [CrossRef]
54. Jannesari, M.; Akhavan, O.; Madaah Hosseini, H.R.; Bakhshi, B. Graphene/CuO_2 nanoshuttles with controllable release of oxygen nanobubbles promoting interruption of bacterial respiration. *ACS Appl. Mater. Interfaces* **2020**, *12*, 35813–35825. [CrossRef]
55. Ahmadpur, M. Impact of COVID-19 spread on road safety indices of Turkey. *Int. J. Inj. Control. Saf. Promot.* **2022**, *29*, 1–12. [CrossRef]
56. Wu, T.; Zhu, X.; Xing, Z.; Mou, S.; Li, C.; Qiao, Y.; Liu, Q.; Luo, Y.; Shi, X.; Zhang, Y.; et al. Greatly improving electrochemical N2 reduction over TiO2 nanoparticles by iron doping. *Angew. Chem. Int. Ed.* **2019**, *58*, 18449–18453. [CrossRef]
57. Khalid, N.R.; Hussain, M.K.; Murtaza, G.; Ikram, M.; Ahmad, M.; Hammad, A. A Novel Ag2O/Fe–TiO2 Photocatalyst for CO2 Conversion into Methane Under Visible Light. *J. Inorg. Organomet. Polym. Mater.* **2019**, *29*, 1288–1296. [CrossRef]
58. Zhang, M.; Wang, S.; Li, Z.; Liu, C.; Miao, R.; He, G.; Zhao, M.; Xue, J.; Xia, Z.; Wang, Y.; et al. Hydrothermal synthesis of MoS_2 nanosheet loaded TiO_2 nanoarrays for enhanced visible light photocatalytic applications. *RSC Adv.* **2019**, *9*, 3479–3485. [CrossRef]
59. Ghorai, T.K.; Chakraborty, M.; Pramanik, P. Photocatalytic performance of nano-photocatalyst from TiO2 and Fe2O3 by mechanochemical synthesis. *J. Alloy. Compd.* **2011**, *509*, 8158–8164. [CrossRef]
60. Aguinaco, A.; Amaya, B.; Ramírez-del-Solar, M. Facile fabrication of Fe-TiO2 thin film and its photocatalytic activity. *Environ. Sci. Pollut. Res.* **2022**, *29*, 23292–23302. [CrossRef] [PubMed]
61. Pan, F.; Zhong, X.; Xia, D.; Yin, X.; Li, F.; Zhao, D.; Ji, H.; Liu, W. Nanoscale zero-valent iron/persulfate enhanced upflow anaerobic sludge blanket reactor for dye removal: Insight into microbial metabolism and microbial community. *Sci. Rep.* **2017**, *7*, srep44626. [CrossRef]
62. Pei, K.; Liu, T. Enhanced Cr (VI) removal with Pb (II) presence by Fe^{2+}-activated persulfate and zero-valent iron system. *Environ. Technol.* **2022**, 1–15. [CrossRef]
63. Mancuso, A.; Sacco, O.; Vaiano, V.; Bonelli, B.; Esposito, S.; Freyria, F.; Blangetti, N.; Sannino, D. Visible Light-Driven Photocatalytic Activity and Kinetics of Fe-Doped TiO_2 Prepared by a Three-Block Copolymer Templating Approach. *Materials* **2021**, *14*, 3105. [CrossRef]
64. Wang, M.; Gao, J.; Zhu, G.; Li, N.; Zhu, R.; Wei, X.; Liu, P.; Guo, Q. One-step solvothermal synthesis of Fe-doped BiOI film with enhanced photocatalytic performance. *RSC Adv.* **2016**, *6*, 106615–106624. [CrossRef]
65. Sakar, M.; Prakash, R.M.; Do, T.-O. Insights into the TiO2-Based Photocatalytic Systems and Their Mechanisms. *Catalysts* **2019**, *9*, 680. [CrossRef]
66. Solano, R.A.; Herrera, A.P.; Maestre, D.; Cremades, A. Fe-TiO2 nanoparticles synthesized by green chemistry for potential application in waste water photocatalytic treatment. *J. Nanotechnol.* **2019**, *2019*, 4571848.
67. Senol, S.D.; Boyraz, C.; Ozugurlu, E.; Gungor, A.; Arda, L. Band Gap Engineering of Mg Doped ZnO Nanorods Prepared by a Hydrothermal Method. *Cryst. Res. Technol.* **2019**, *54*, 1800233. [CrossRef]

68. Azarpira, H.; Sadani, M.; Abtahi, M.; Vaezi, N.; Rezaei, S.; Atafar, Z.; Mohseni, S.M.; Sarkhosh, M.; Ghaderpoori, M.; Keramati, H.; et al. Photo-catalytic degradation of triclosan with UV/iodide/ZnO process: Performance, kinetic, degradation pathway, energy consumption and toxicology. *J. Photochem. Photobiol. A Chem.* **2018**, *371*, 423–432. [CrossRef]
69. Ahadi, S.; Moalej, N.S.; Sheibani, S. Characteristics and photocatalytic behavior of Fe and Cu doped TiO2 prepared by combined sol-gel and mechanical alloying. *Solid State Sci.* **2019**, *96*, 105975. [CrossRef]
70. Liu, L.; Chen, F.; Yang, F.; Chen, Y.; Crittenden, J. Photocatalytic degradation of 2,4-dichlorophenol using nanoscale Fe/TiO2. *Chem. Eng. J.* **2011**, *181–182*, 189–195. [CrossRef]
71. Aziz, K.H.H.; Miessner, H.; Mueller, S.; Mahyar, A.; Kalass, D.; Moeller, D.; Khorshid, I.; Rashid, M.A.M. Comparative study on 2,4-dichlorophenoxyacetic acid and 2,4-dichlorophenol removal from aqueous solutions via ozonation, photocatalysis and non-thermal plasma using a planar falling film reactor. *J. Hazard. Mater.* **2018**, *343*, 107–115. [CrossRef]
72. Neghi, N.; Kumar, M. Performance analysis of photolytic, photocatalytic, and adsorption systems in the degradation of metronidazole on the perspective of removal rate and energy consumption. *Water Air Soil Pollut.* **2017**, *228*, 1–12.
73. Available online: https://www.info.gov.hk/gia/general/202111/09/P2021110900485.htm (accessed on 25 April 2022).